PHOTONICS Research

Chip-integrated plasmonic flat optics for mid-infrared full-Stokes polarization detection

Jing Bai,[1,2] Chu Wang,[1,2] Xiahui Chen,[1,2] Ali Basiri,[1,2] Chao Wang,[1,2,3] and Yu Yao[1,2,*]

[1]School of Electrical, Computer and Energy Engineering, Arizona State University, Tempe, Arizona 85281, USA
[2]Center for Photonic Innovation, Arizona State University, Tempe, Arizona 85281, USA
[3]Biodesign Center for Molecular Design & Biomimetics, Arizona State University, Tempe, Arizona 85281, USA
*Corresponding author: yuyao@asu.edu

Received 18 March 2019; revised 1 July 2019; accepted 19 July 2019; posted 24 July 2019 (Doc. ID 361172); published 22 August 2019

Flat optics presents a new path to control the phase, amplitude, and polarization state of light with ultracompact devices. Here we demonstrate chip-integrated metasurface devices for polarization detection of mid-infrared light with arbitrary polarization states. Six high-performance microscale linear and circular polarization filters based on vertically stacked plasmonic metasurfaces (with total thickness <600 nm) are integrated on the same chip to obtain all four Stokes parameters of light with high accuracy. The device designs can be tailored to operate at any wavelength in the mid-infrared spectral region and are feasible for on-chip integration with mid-infrared (mid-IR) photodetectors and imager arrays. Our work will enable on-chip mid-IR polarimeters and polarimetric imaging systems, which are highly desirable for many applications, such as clinical diagnosis, target detection, and space exploration.

https://doi.org/10.1364/PRJ.7.001051

1. INTRODUCTION

Polarization state is one of the most important properties of light and essential for applications such as communication [1,2], remote sensing [3], astronomy [4], polarization imaging [5], polarization navigation [6–8], chemical analysis [9], and biomedical diagnosis [10–12]. Polarization detection in the mid-infrared (mid-IR) spectral range (3–12 μm) is especially attractive due to its broad applications in molecular spectroscopy [13,14], biomedical diagnosis [15,16], target detection [17,18], and face recognition [18,19]. Conventional mid-IR polarization detection methods require rotating optical components, which are bulky and difficult for device integration and miniaturization [19–21]. Moreover, these systems are also limited in measurement speed and accuracy of polarization state; therefore, it is highly desirable, though challenging, to realize mid-IR polarimetric detection using a compact and economic system. Monolithically integrated polarimetric imaging systems in visible and IR wavelength ranges have been demonstrated [22–25] by stacking micropolarization filters on top of silicon photodetectors. In these devices, the incoming light is filtered by the spatially distributed microscale polarizers before being collected by the imaging detectors. Such a spatial division measurement scheme avoids the requirement of moving parts, which makes on-chip integration much easier and reliable. The spatial division approach requires four to six different types of polarization filters, including both linear polarization (LP) and circular polarization (CP) filters, to measure the polarization state of light at each pixel. Various types of polarization filters have been used, such as birefringent materials [22], thin-film polarizers [23–26], and metallic nanowires [27–29]. Yet the applications of these polarimetric imaging systems are hindered by various limitations. Methods based on organic materials, such as liquid crystal polymer [30,31] and chiral organic molecules [32], are incompatible with scalable manufacturing technology, structurally and chemically unstable, and highly absorptive in mid-IR spectral regions. On the other hand, polarimetric imaging sensors utilizing metallic nanowires [21,27–29] as LP filters have been proven feasible from visible to mid-IR wavelength ranges; however, these devices are not suitable for complete polarization state (full-Stokes) measurement due to the lack of CP filters.

Recently, flat optics based on metamaterials and metasurfaces opens a new path for on-chip polarization detection as a result of the ultracompact form factors, great design flexibility, and broad wavelength coverage [33–41]. Among these designs, artificial three-dimensional (3D) chiral plasmonic metamaterials in the forms of helical and spiral shapes [33,34] can differentiate the handedness of circularly polarized light (CPL) with a circular polarization extinction ratio (CPER) up to 15 but face serious challenges in scalable manufacturing due to structural complexity. In comparison, CP filters made of planar metasurfaces, such as gammadions [35], Z-shaped antennas [36], nanoslits [39], and twist-stacked multiple-layer structures (crosses [38], nanorods [40,41], etc.), are more suitable for scalable fabrication, yet with relatively low CPER (<8). Moreover, planar

metasurface structures, such as phase-gradient nanoantenna arrays [42,43], plasmonic aperture antennas [39], and dielectric metasurfaces [44–46], have also been designed to realize full-Stokes polarization detection in visible and near IR wavelength regions. Among these designs, dielectric metasurfaces provide the best efficiencies, yet scaling up the operation wavelength to the mid-IR wavelength range would require growth and etching of thick dielectric layers, which can be challenging for device fabrication and integration. Phase-gradient nanoantenna arrays are most promising for extending into the mid-IR wavelength range because they have demonstrated the best polarization measurement accuracy (measurement errors of Stokes parameters ~10%) [42,43] and broad operation bandwidth (200–300 nm); however, these devices work in reflection/diffraction mode and thus are challenging for direct integration onto photodetectors and imaging sensors. More recently, polarization detection based on electrically tunable graphene-integrated metasurfaces has been demonstrated at mid-IR (6.8 μm) [47]; yet the devices still work in reflection mode and thus are not feasible for monolithic integration on photodetectors and imaging sensors. To date, the realization of on-chip mid-IR polarimetric detection and imaging arrays remains elusive.

Here we demonstrate experimentally full-Stokes polarization detection in the mid-IR wavelength range based on chip-integrated plasmonic metasurfaces operating in transmission mode. We have adopted the spatial division scheme and implemented six micrometer-size metasurface polarization filters, including both LP and CP filters, on the same chip to measure the full-Stokes parameters of incident light with arbitrary polarization. Our design is featured with an ultracompact form factor and high measurement accuracy and capability of monolithic integration onto a variety of mid-IR photodetectors and imaging arrays.

2. DEVICE DESIGN

The polarization detector design proposed here [Fig. 1(a)] is based on a spatial division measurement scheme. It is composed of six spatially distributed microscale polarization filters (P_1 to P_6) and one unstructured cell (P_0) without any filter. All seven cells have the same area. The unstructured cell is used to transmit the total intensity of incident light I_0. The LP filters

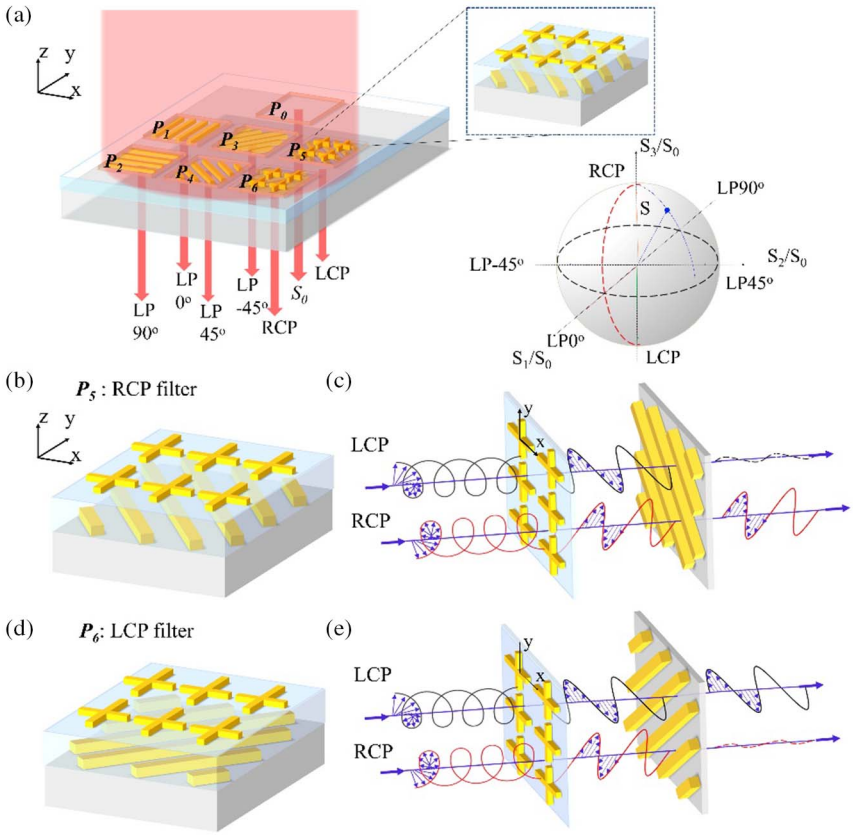

Fig. 1. Mid-IR full-Stokes polarization detection. (a) Schematic of the device design with seven cells for direct Stokes parameter measurement. P_0 is the reference cell to measure the total light intensity. P_1–P_4 cells are LP filters to filter linearly polarized light with the electric field vector oriented at different angles with respect to the *x*-axis, i.e., LP = 0°, 90°, −45°, and 45°. P_5–P_6 cells are RCP and LCP filters, respectively. The inset shows the schematic of the LCP filter. On the Poincaré sphere (right panel), *S* indicates an arbitrary polarization state. (b) Schematic of the RCP filter consisting of a top metasurface QWP and an underneath nanograting LP filter. (c) The working principle of the RCP filter. The metasurface QWP converts the incident RCP (LCP) light to LP light, which is selectively transmitted (blocked) by the nanograting LP filter. (d) Schematic of the chip-integrated LCP filter with similar structure to the RCP filter. (e) The working principle of the LCP filter. The metasurface QWP converts the incident LCP (RCP) light to LP light, which is selectively transmitted (blocked) by the nanograting LP filter.

(P_1, P_2, P_3, and P_4) are based on metallic nanogratings oriented in four different directions to pass LP components oriented 0°, 90°, −45°, and 45° with respect to x-axis, respectively. Two CP filters (P_5 and P_6) transmit right-handed circular polarization (RCP) and left-handed circular polarization (LCP), respectively.

By detecting the transmitted light intensity through each cell separately, one can retrieve all the polarization components in the input light. The Stokes parameters (S_0, S_1, S_2, and S_3) of the input light can be calculated as [48]

$$\begin{cases} S_0 = I_0, \\ S_1 = I_{0^\circ} - I_{90^\circ}, \\ S_2 = I_{45^\circ} - I_{-45^\circ}, \\ S_3 = I_{\mathrm{RCP}} - I_{\mathrm{LCP}}, \end{cases} \tag{1}$$

where I_{0°, I_{90°, I_{45°, and I_{-45° are the intensities of linear polarization components along 0°, 90°, 45°, and −45° with respect to x-axis. I_{RCP} and I_{LCP} are the intensities of right-handed circularly polarized light and left-handed circularly polarized light, respectively.

Such a device design can enable detecting an arbitrary polarization state of the incident light, including partially polarized light [1]. The Stokes parameters satisfy the relation $S_1^2 + S_2^2 + S_3^2 = S_0^2$ for fully polarized light and $S_1^2 + S_2^2 + S_3^2 < S_0^2$ for partially polarized light. To perform complete measurement of the arbitrary polarization states with high accuracy, one needs to realize four LP and two CP polarization filters with high extinction ratios. In the following, we will present the design and experimental demonstration of individual polarization filters, followed by the overall performance characterization of Stokes parameter detection of light with an arbitrary polarization state.

While the design and fabrication of LP filters such as metallic nanogratings are straightforward, chip-integratable CP filters in mid-IR wavelength range with high CP extinction ratio (CPER) are much more challenging to realize. Here, inspired by the extraordinary CP light vision of Stomatopods (or mantis shrimps) [49,50], we design mid-IR CP filters with high CPER based on ultrathin double-layer plasmonic metasurfaces ($\lambda_0/4 - \lambda_0/7$). The CP light vision of Stomatopods originates from the unique structures of their compound eyes [50,51]. In each compound eye, a top retinular cell and seven bottom retinular cells form a natural CP filter. The top retinular cell acts as a quarter-wave plate (QWP) to convert CPL to linearly polarized light (LPL) while the microvilli of bottom retinular cells function as wire-grid polarizers, which are oriented 45° with respect to the long axis of the QWP. Inspired by such a simple configuration, we designed bio-inspired right-handed circular polarization and left-handed circular polarization filters based on vertically integrated metasurfaces, as shown in Figs. 1(b) and 1(d). Both the RCP and LCP filters have two key elements, i.e., a plasmonic metasurface QWP composed of cross-shaped antennas to mimic the top retinular cell and a nanograting LP filter to mimic the bottom retinular cells. By vertically integrating the two layers of achiral planar plasmonic structures, we create a chiral plasmonic structure, which is not superimposable on its mirror image. For RCP filter design [Fig. 1(c)], the input RCP (LCP) light is first converted to LPL oriented at an angle of 45° (−45°) with respect to the x-axis via the metasurface QWP. Then the nanograting LP filter selectively transmits the LPL oriented at 45° while blocking the LPL oriented at −45°, thus resulting in a much higher transmission for RCP than LCP light. For the LCP filter, the plasmonic metasurface QWP remains the same but the nanograting polarizer is instead oriented at a 45° angle with respect to the x-axis, leading to a much higher transmission for LCP than RCP light.

The plasmonic metasurface QWPs are designed based on the fact that an abrupt phase shift is introduced between the incident light and scattered light when light interacts with optical antennas. The phase shift is wavelength-dependent and can be controlled by engineering the antenna geometry [52]. Here the metasurface QWPs are composed of cross-shaped antennas with different arm lengths [Fig. 2(a)]. For incident electric fields E_x and E_y, the resonance "dips" in the transmission spectra [Fig. 2(b)] correspond to the first-order resonance modes for the linear antennas oriented along x- and y-axes, respectively. Due to the different resonance wavelengths, the scattered fields along the two axes experience different phase shifts, especially in the wavelength region between the two antenna resonances.

By engineering the dimension of the cross-shaped antenna array, we can introduce a $\pi/2$ phase difference between E_x and E_y with the same transmission coefficients at the wavelengths roughly in the middle of the two antenna resonances. The bottom panel in Fig. 2(b) shows the phase difference introduced by the wavelengths roughly in the middle of the two antenna resonances. The bottom panel in Fig. 2(b) shows the phase difference introduced by the metasurface QWP calculated via full-wave finite difference time-domain (FDTD) simulation for an operation wavelength of around 3.8 μm. The operation wavelength of the metasurface QWP can be engineered from mid-IR (MIR) to near-IR (NIR) by changing the geometric parameters of the cross-shaped antenna (see Appendix A for more details). The nanograting polarizers are designed to provide a high linear polarization extinction ratio (LPER), i.e., $r_{\mathrm{LP}} = T_u/T_v$, as indicated in Fig. 2(c). We have designed a gold nanograting LP filter with an LPER > 1000 at ∼3.8 μm and 90% transmission of selected LPL (T_u) for wavelengths longer than 1.5 μm. Even higher LPER can be achieved by engineering the nanograting design parameters, such as the grating duty cycle and thickness.

The double-layer plasmonic CP polarization filters [Fig. 2(a)] are composed of a gold plasmonic metasurface QWP, a gold nanograting LP filter, and a dielectric spacer layer (silicon oxide) between them. The thickness of the spacer layer is chosen to maximize the CPER of the device (see more details in Appendix C). Meanwhile, the separation between the metasurface QWP and the nanograting LP filter ensures that the near-field interaction between the two plasmonic layers does not significantly change their optical response. Moreover, it also helps to smooth the surface of the nanogratings to facilitate subsequent integration of the QWP on top. We also investigated the impact of the lateral displacement between the metasurface QWP and nanograting LP filter. Full simulation results show that our device designs do not rely on accurate alignment between the two to realize high CPER performance (see more

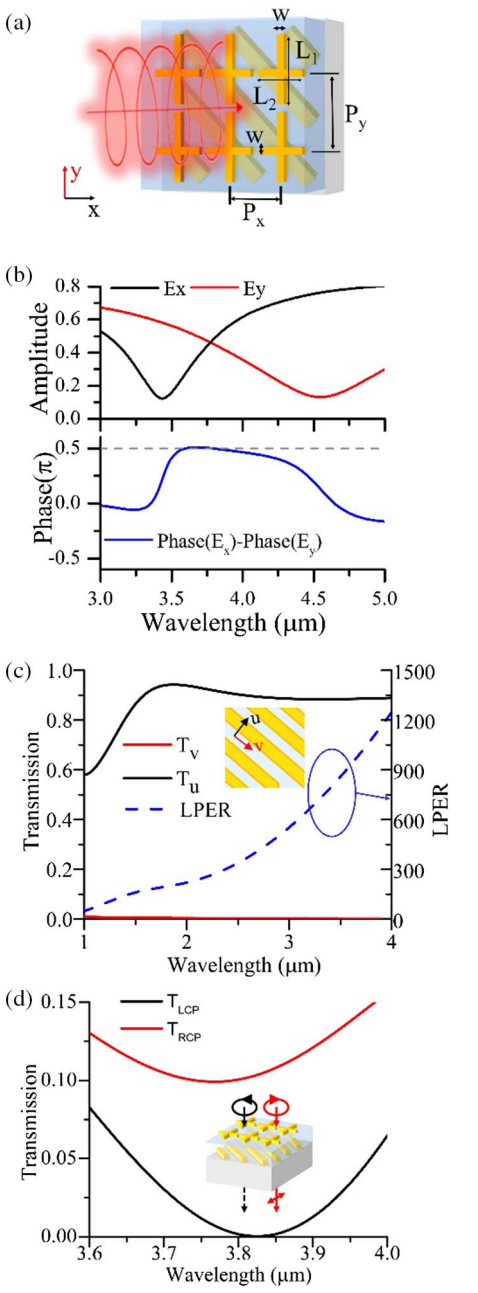

Fig. 2. Circular polarization filter design. (a) A schematic of the RCP filter. (b) Calculated amplitude and phase difference of electric field components of the transmitted light along two orthogonal arms of the crossbar metasurface (thickness 40 nm). The design parameters are as follows: $L_1 = 1.55$ μm, $L_2 = 1.04$ μm, $P_x = 1.24$ μm, $P_y = 1.68$ μm, and $W = 140$ nm. (c) Transmission spectra of nanogratings for input light polarized perpendicularly (black solid line, polarization along 45° to the x-axis, i.e., the u-axis in the inset) or parallel (red solid line, along −45° to x-axis, i.e., v-axis in the inset) to the nanogratings (thickness 120 nm, period 200 nm, and duty cycle 50%) and the corresponding linear polarization extinction ratio (blue dashed line). (d) Transmission spectra of LCP (black) and RCP (red) light through the RCP polarization filter. The inset shows that RCP input is transmitted but LCP input is blocked. The design parameters for the crossbar antenna are as follows: $L_1 = 1.55$ μm, $L_2 = 1.17$ μm, $P_x = 1.343$ μm, $P_y = 2.015$ μm, and $W = 140$ nm. The thickness of the oxide spacer layer is 350 nm. The nanogratings have the same design parameters as those in (c).

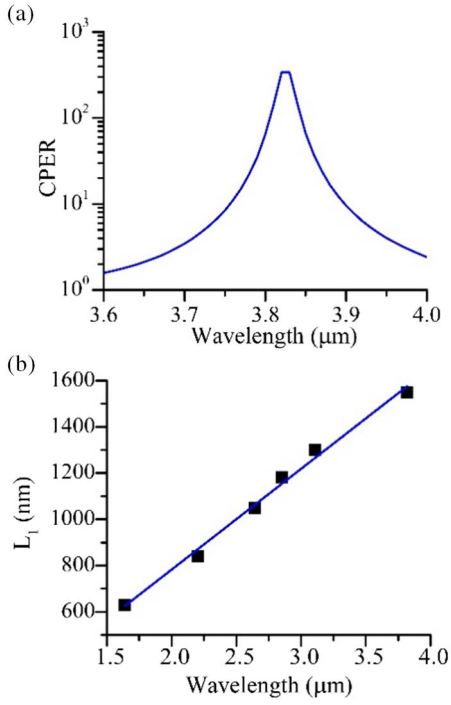

Fig. 3. Circular polarization filter performance and wavelength engineering. (a) The extinction ratio of an RCP filter ($r_{CP} = T_{RCP}/T_{LCP}$) designed at wavelength ~3.8 μm. Same design dimensions as Fig. 2(d). (b) Operation wavelength engineering of the CPL filters with different antenna length L_1. The solid blue line is a linear fit of the data points (black squares) obtained with full-wave simulation (FDTD). More detailed information about the design parameters and simulation results is provided in Appendix B.

details in Appendix D), which reduces the complexity of device fabrication. The total thickness of the whole structure is close to 600 nm, about one-sixth of the operational wavelength. Figure 2(d) shows the transmission spectra of RCP and LCP input light for an RCP filter designed at an optimal operation wavelength of 3.8 μm. The extracted CPER reaches a maximum value of over 300 and provides high CPER (>10) over a bandwidth of 150 nm [Fig. 3(a)]. The operational wavelength of the CP filters can be engineered by changing the geometric parameters of the structure. Figure 3(b) shows the tuning of operational wavelengths from 1.6 to 3.8 μm as a function of the longer arm length (L_1) of the cross-shaped antenna (see more details in Appendix B).

3. EXPERIMENTAL RESULTS

We first fabricated the CPL filters on sapphire substrates, which have a mid-IR transmission cutoff wavelength (around 5 μm) longer than the designed operational wavelengths. The fabrication process is illustrated in Fig. 4(a). First, gold nanogratings with 200 nm period, 50% duty cycle, and 120 nm thickness were patterned on the substrate with electron beam lithography (EBL), metal film deposition (Cr/Au 5/120 nm), and metal lift-off. Figure 4(b) shows a scanning electron microscopy (SEM) image of the fabricated nanogratings. After solvent cleaning and brief Ar plasma cleaning, a 350 nm thick silicon oxide spacer

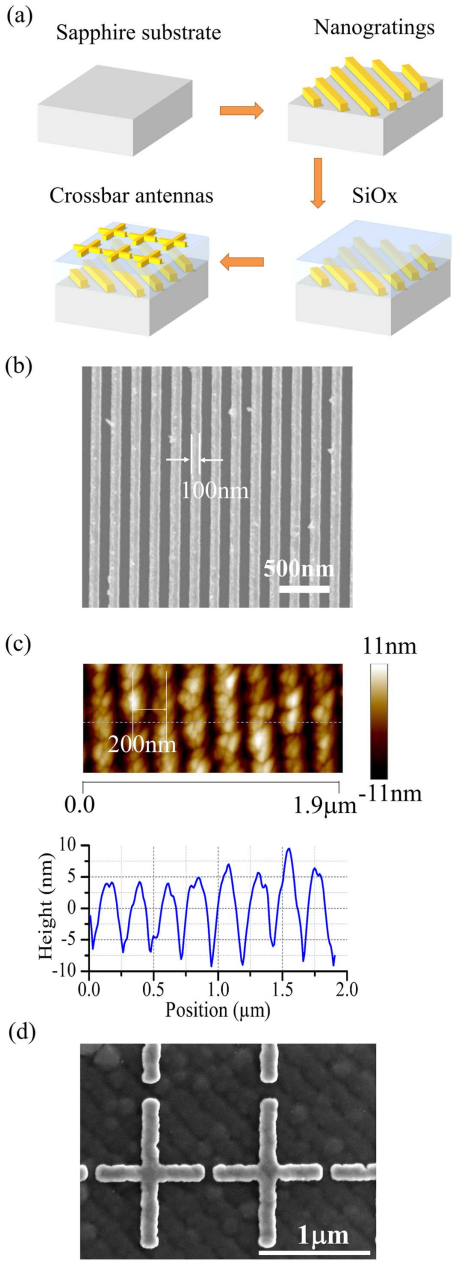

Fig. 4. Device fabrication process. (a) Major steps in device fabrication of CP polarization filter: (1) nanograting patterning on a sapphire substrate, (2) SiO_x deposition by sputtering, and (3) crossbar antenna patterning. (b) An SEM image of nanogratings before SiO_x deposition. (c) Top panel: an AFM image of a nanograting covered by SiO_x. Bottom panel: the height profile along the white dashed line in the AFM image. (d) An SEM image of a fabricated mid-IR RCP filter.

layer was deposited on top of the nanogratings via a sputtering process. Atomic force microscopy (AFM) images of the nanogratings covered by the oxide spacer layer [Fig. 4(c)] indicate a dramatically reduced surface roughness ($R_a = 4.88$ nm). The greatly reduced surface roughness facilitates the subsequent integration of plasmonic metasurface QWP. The metasurface QWPs were fabricated on top of the nanogratings by EBL, metal deposition (Cr/Au 3/50 nm), and lift-off. Figure 4(d) shows an SEM image of fabricated CPL polarization filters for an operation wavelength around 4 μm.

We characterized the metasurface CPL filters with a setup as illustrated in Fig. 5(a). Unpolarized light from a Fourier transform infrared spectrometer (FTIR) first passed through a linear polarizer and a QWP to generate CPL (at wavelengths close to 4 μm). The handedness of CPL was controlled by adjusting the angle between the optical axes of the linear polarizer and the QWP. The measured transmission spectra for LCP and RCP incident light of a fabricated RCP filter are shown in Fig. 5(b). The extracted CPER is over 16 at the best operational wavelength (~4 μm), as shown in Fig. 5(c). Our device provides high CPER (>10) over a wavelength range of 300 nm (from 3.8 to 4.1 μm). The relatively lower transmission (~10%) of the selected polarization state compared to simulated results [Fig. 2(d)] is likely due to higher loss introduced in the plasmonic metasurface QWP and nanogratings as a result of the structural deviations of fabricated devices from the optimal design parameters. There is still much room to further improve the performance of the CP filters by taking into account the difference in material parameters between simulation and experiments as well as more accurate control of structure geometries.

To demonstrate complete polarization state detection, we integrated both CP polarization filters and four LP filters on the same substrate [Fig. 1(a)]. The polarization detection was performed with the setup shown in Fig. 6(a). The output light from FTIR (unpolarized) first passed through a linear polarizer and a QWP. The polarization state of light (at the operation wavelength around 4 μm) was controlled by rotating the linear polarizer and the QWP. A reflective condenser was used to focus light on the device. To avoid the impacts of the condenser on the polarization state of light, the QWP was placed between the condenser and the device under test. The transmitted light through the sample was then collected by an MCT photodetector, with the region of interest selected by an aperture placed at the conjugated image plane. Such a setup allowed us to characterize light transmission through microscale areas down to 20 μm × 20 μm with sufficient signal to noise ratio (SNR) (see Appendix E). To precisely determine the generated polarization state, we first calibrated all LP and CP filters to obtain their transmission efficiencies and extinction ratios for each filter. Then polarization measurements were carried out for input light with arbitrary polarization states. For each polarization state, the transmitted light of all filters was measured sequentially by controlling the lateral displacement of the motorized stage. As discussed previously [Fig. 1(a)], we obtained all the polarization components of the input light to achieve all four Stokes parameters. To determine the accuracy of the measured Stokes parameters, we replaced our device with a rotating linear polarizer as a polarization analyzer (PA) to obtain the Stokes parameters as a reference (see more details in Appendix F). Since all generated light was purely polarized, we were able to obtain both polar plots [left panels in Figs. 6(b)–6(d)] and polarization ellipse plots for a number of input polarization states [right panels in Figs. 6(b)–6(d), more polarization states provided in the Appendix F]. The measurement results obtained by our device (red lines) agreed well with

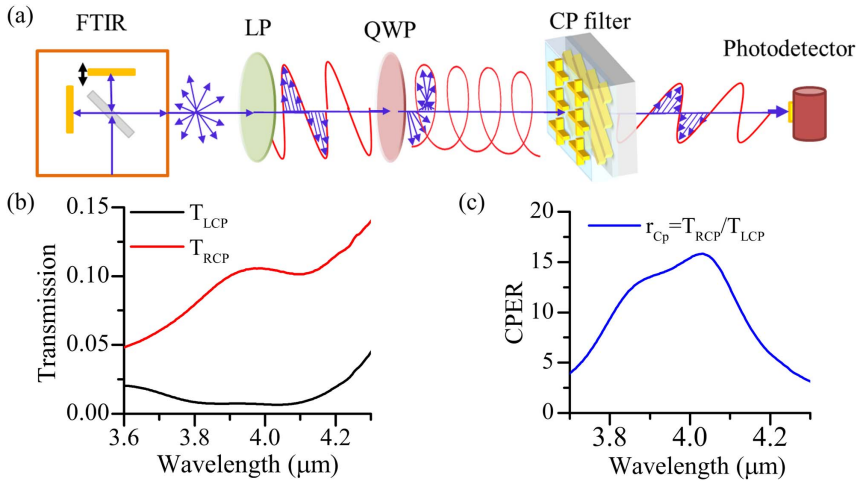

Fig. 5. Experimental setup and measurement results of CP filters. (a) A schematic of the measurement setup for CP filter characterization. (b) Transmission spectra for a mid-IR RCP filter with RCP (red) and LCP (black) input. (c) The extracted CPER ($r_{CP} = T_{RCP}/T_{LCP}$) for the RCP filter designed for an operation wavelength around 4 μm.

reference results (black circles) measured by the rotating PA. The blue arrows on the ellipse plots indicate the handedness of the circularly and elliptically polarized light determined with our device, which is not available from the measurement taken by the rotating PA. Based on all nine polarization states we have characterized, the average errors for orientation angle and elliptical angle are 1.2° and 1.9°, respectively. Figure 6(e) shows the measured Stokes parameters (normalized by S_0) with our device and those obtained by rotating PA for nine polarization states. The average errors of S_1 and S_2 are 0.035 and 0.025, respectively. The average error of S_3 is 0.104, which is limited by the CPERs of the CP filters. From the measurement results of the Stokes parameters, we also extracted the average measurement error for DOLP and DOCP to be 2.3% and 10.3%, respectively.

To the best of our knowledge, our devices exhibit the best polarization measurement accuracy among all structures in the literature so far [42–45]. The measurement accuracy can be further improved via increasing the extinction ratio of all micropolarization filters and reducing the insertion loss. As a proof of concept demonstration, we use a motorized stage to characterize our device. The CP and LP filters demonstrated here operate in transmission mode and can be monolithically integrated onto various mid-IR photodetector arrays and imager arrays to achieve on-chip polarimeter and polarimetric imaging sensors, where the incident light is filtered by the LP and CP filters and then collected by the photodetectors beneath them. Thus, these chip-integrated devices can perform full-Stokes polarization detection and capture polarimetric images without moving parts.

4. CONCLUSION

In this paper, we present theoretical modeling and experimental demonstration of complete mid-IR polarization detection with a microscale filter array based on subwavelength-thick plasmonic metasurfaces. Unlike conventional polarization detectors requiring bulky and complex systems, our design can be fabricated monolithically on a single chip with a total device layer thickness of about 600 nm. We experimentally demonstrated full-Stokes parameter detection for arbitrary polarization at mid-IR wavelengths with the best measurement accuracy reported in the literature so far, to the best of our knowledge. Additionally, the design concepts can be applicable over a broad wavelength range by engineering the design parameters and thus are promising for multi-wavelength or broadband polarization detection. Moreover, the metasurface device design is compatible with conventional semiconductor substrates, such as silicon, III-V, and II-VI semiconductors and can be integrated with photodetector arrays on the same chip. Therefore, our technique has great potential to enable mid-IR on-chip polarimetric imaging systems and polarimeters, which are highly desirable for many applications, such as biomedical imaging, target detection, material characterization, and molecular spectroscopy.

APPENDIX A: OPERATION WAVELENGTH ENGINEERING OF THE METASURFACE QWP

The operation wavelength of the metasurface QWP can be engineered by changing the design parameters. One of the critical requirements to design a QWP is introducing a $\pi/2$ phase difference between two orthogonal electric field components with equal amplitude (i.e., E_x and E_y). FDTD simulations are performed to optimize different metasurface QWP designs with operational wavelengths from NIR to MIR by scaling the geometric dimensions of the metasurface QWP (Fig. 7). The corresponding design parameters of the metasurface QWP at different wavelengths are shown in Fig. 8.

APPENDIX B: WAVELENGTH ENGINEERING OF METASURFACE CPL FILTERS

FDTD simulations are performed to optimize CPL filter designs at operation wavelengths from 1.6 to 3.8 μm.

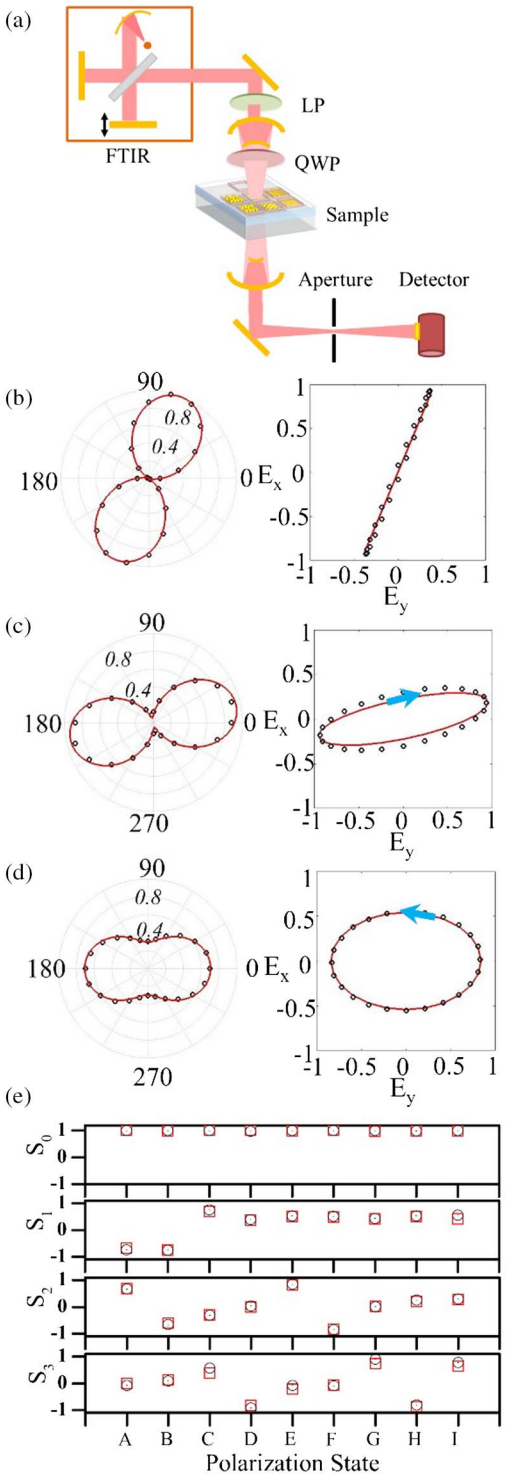

Fig. 6. Full-Stokes polarization measurements. (a) Schematic of the measurement setup. Unpolarized light from the FTIR is converted to polarized light with an arbitrary polarization state by adjusting the orientation of the standalone linear polarizer and the QWP. Then the light is transmitted through our device placed on a motorized stage and finally collected by the detector. (b)–(d) Polar plots and ellipse plots for polarization states A, C, and D in (e) (black circle: measured from polarization analyzer; red solid: measured from our Stokes parameter detector). (e) Measured Stokes parameters for nine polarization states (black circles: polarization states of input light; red squares: measured results with our device).

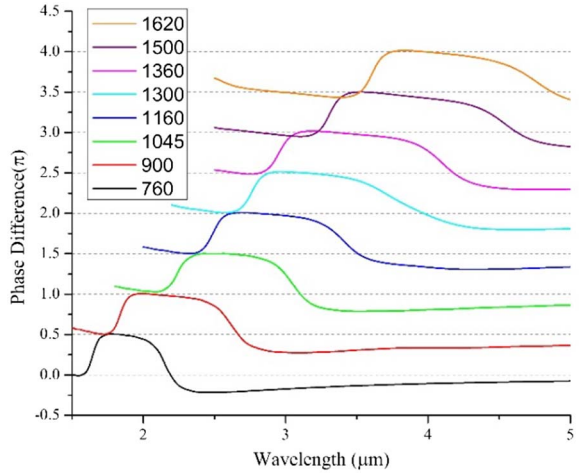

Fig. 7. Phase difference of the transmitted light along two orthogonal arms of the QWP metasurface with the length of the longer arm, $L_1 = 700$, 900, 1045, 1160, 1300, 1360, 1500, and 1620 nm. Other design parameters are scaled accordingly.

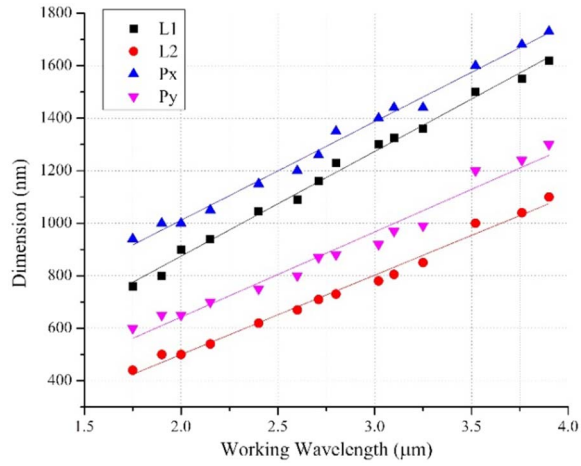

Fig. 8. Geometric dimensions of the metasurface QWP with working wavelengths covering from NIR to MIR. L_1 is the length of the longer arm along the y-axis, and L_2 is the length of the shorter arm along the x-axis. P_x is the period in the x-direction and P_y is the period in the y-direction.

The extinction ratios of six LCP filters for different wavelengths are shown in Fig. 9.

APPENDIX C: SPACER LAYER THICKNESS AND DEVICE PERFORMANCE

We performed full-wave simulations to determine the spacer layer thickness for the highest CPER (Fig. 10). The dependence of device performance on the spacer layer thickness is mainly due to the multiple reflections at the top metasurface layer (QWP) and the bottom grating layer (linear polarizer).

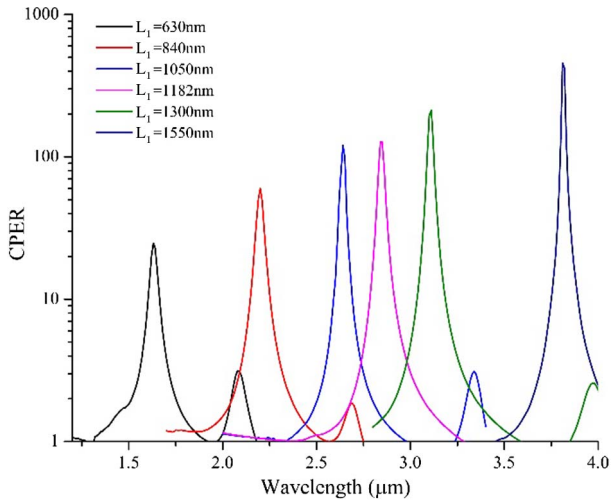

Fig. 9. Extinction ratio ($r_{CP} = T_{LCP}/T_{RCP}$) for six LCP filters mentioned in Fig. 3(b). The other design parameters of the cross-bar antennas are as follows: $L_2 = 0.42$, 0.58, 0.73, 0.82, 0.9, and 1.17 μm; and $W = 100$, 100, 112, 127, 140, and 140 nm. The nano-gratings have the same design parameters as those in Fig. 2(c). The thickness of the oxide spacer is 220 nm for the device at 1.6 μm and 350 nm for all the other designs.

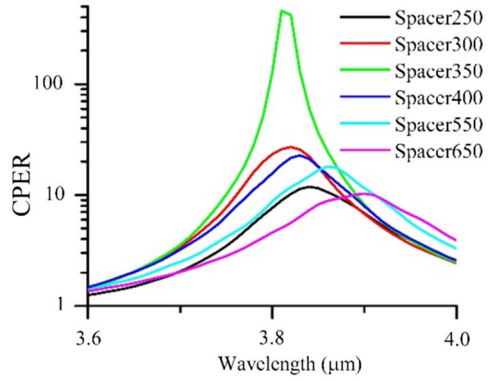

Fig. 10. CPER for LCP filters with various spacer layer thicknesses. The other design parameters are the same as those used for the structure in Fig. 2(d).

APPENDIX D: LATERAL DISPLACEMENT AND DEVICE PERFORMANCE

We investigated the influence of the lateral displacement between the top metasurface QWPs and the bottom nanogratings [illustrated in Fig. 11(a)]. According to full-wave simulation results, the CPERs of the device around the operation wavelength remained higher than 200 [Fig. 12(a)], when the displacement between the QWP and the nanogratings linear polarizer was shifted over 200 nm along the y-axis.

APPENDIX E: CPL FILTER CHARACTERIZATION AND STOKES PARAMETER DETECTION

For CP filter characterization, a linear polarizer and a mid-IR QWP (Thorlabs, WPLQ05M-4000) were used to generate CP

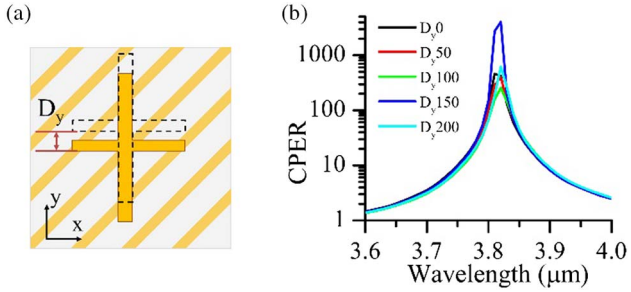

Fig. 11. (a) Schematic for the MIR LCP filter with 0–200 nm lateral displacement along the y-axis. (b) CPER ($r_{CP} = T_{LCP}/T_{RCP}$) for the MIR LCP filter with 0–200 nm lateral displacement along y-axis. The other design parameters are the same as those in Fig. 2(d).

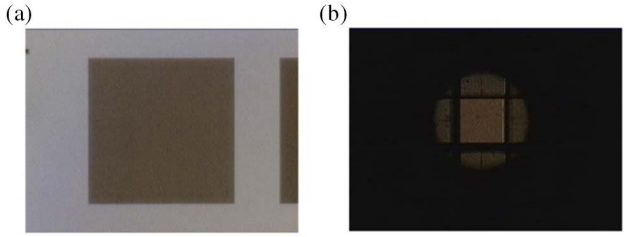

Fig. 12. (a) Microscope image of the CPL filter (160 μm × 160 μm) without an aperture. (b) Microscope image of the CPL filter with an input aperture (100 μm in diameter) and an aperture at the image plane (50 μm × 50 μm).

states, which were verified by a rotating linear polarizer. Then the generated CP light was transmitted through the device under test, collected by an objective (15×), and detected by an MCT detector. An aperture (a built-in feature of HYPERION Series FTIR Microscopes, Bruker Inc.) of 50 μm × 50 μm at the image plane in front of the MCT detector was used to select the measurement area on the device (Fig. 12).

For Stokes parameter detection, the transmission coefficients of the CP and LP filters were first calibrated with CP and LP input light, respectively. Then the input linear polarizer and QWP were rotated to generate arbitrary polarization states of light. The transmitted light through each of the seven detection units [Fig. 1(a)] was sequentially measured utilizing the aperture and the computer-controlled motorized stage. The transmitted light through each filter was divided by the corresponding calibration data to consider different transmission coefficients of the polarization filters. We also characterized the generated polarization states with a rotating linear polarizer to obtain the reference data. Note that with only one linear polarizer, one can only measure the linear components of Stokes parameters S_1 and S_2 but not S_3, the sign of which indicates the handedness of polarized light. In order to obtain S_3, both the QWP and the linear polarizer are required as rotation components, which is not feasible for us due to the space limitation of our setup.

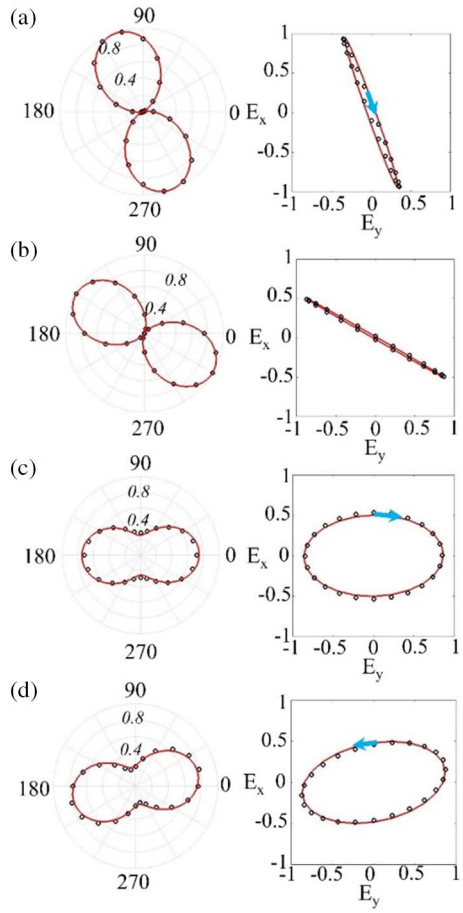

Fig. 13. Stokes parameters measurement results for four polarization states, which correspond to the data points B, F, G, and H in Fig. 6(e). Black circles: measured with PA; red solid line: measured with our device. Blue arrows indicate the handedness of the polarization state.

APPENDIX F: STOKES PARAMETERS DETECTION RESULTS

Besides the experiment results for Stokes parameters detection shown in Figs. 6(b)–6(d), the measurement results for other polarization states are shown [Figs. 13(a)–13(d)]. The polar plots and the ellipse plots correspond to B, F, G, and H in Fig. 6(e).

Funding. U.S. Air Force (FA9550-16-1-0183); Directorate for Engineering (1542160, 171141, 1809997); National Science Foundation (NSF) (ECCS-1542160); Arizona State University.

Acknowledgment. The devices were fabricated in the NanoFab and Eyring Materials Center (EMC) at Arizona State University. P. Amrollahi from Arizona State University participated in the device fabrication for SiO_2 sputtering. Y. Yao and C. Wang acknowledge support from Arizona State University.

REFERENCES

1. Y. Han and G. Li, "Coherent optical communication using polarization multiple-input-multiple-output," Opt. Express **13**, 7527–7534 (2005).
2. X. Zhao, Y. Yao, Y. Sun, and C. Liu, "Circle polarization shift keying with direct detection for free-space optical communication," J. Opt. Commun. Netw. **1**, 307–312 (2009).
3. N. J. Pust and J. A. Shaw, "Digital all-sky polarization imaging of partly cloudy skies," Appl. Opt. **47**, H190–H198 (2008).
4. K. Ichimoto, B. Lites, D. Elmore, Y. Suematsu, S. Tsuneta, Y. Katsukawa, T. Shimizu, R. Shine, T. Tarbell, A. Title, J. Kiyohara, K. Shinoda, G. Card, A. Lecinski, K. Streander, M. Nakagiri, M. Miyashita, M. Noguchi, C. Hoffmann, and T. Cruz, "Polarization calibration of the solar optical telescope onboard Hinode," in *The Hinode Mission*, T. Sakurai, ed. (Springer, 2008), pp. 179–207.
5. F. Snik, J. Craven-Jones, M. Escuti, S. Fineschi, D. Harrington, A. D. Martino, D. Mawet, J. Riedi, and J. S. Tyo, "An overview of polarimetric sensing techniques and technology with applications to different research fields," Proc. SPIE **9099**, 90990B (2014).
6. D. Wang, H. Liang, H. Zhu, and S. Zhang, "A bionic camera-based polarization navigation sensor," Sensors **14**, 13006–13023 (2014).
7. M. Sarkar, D. S. S. Bello, C. Van Hoof, and A. Theuwissen, "Biologically inspired autonomous agent navigation using an integrated polarization analyzing CMOS image sensor," Procedia Eng. **5**, 673–676 (2010).
8. J. Chu, K. Zhao, Q. Zhang, and T. Wang, "Construction and performance test of a novel polarization sensor for navigation," Sens. Actuators A Phys. **148**, 75–82 (2008).
9. L. A. Nafie and T. B. Freedman, "Vibrational circular dichroism: an incisive tool for stereochemical applications," Enantiomer **3**, 283–297 (1998).
10. B. Kunnen, C. Macdonald, A. Doronin, S. Jacques, M. Eccles, and I. Meglinski, "Application of circularly polarized light for non-invasive diagnosis of cancerous tissues and turbid tissue-like scattering media," J. Biophoton. **8**, 317–323 (2015).
11. E. Salomatina-Motts, V. A. Neel, and A. N. Yaroslavskaya, "Multimodal polarization system for imaging skin cancer," Opt. Spectrosc. **107**, 884–890 (2009).
12. R. Patel, A. Khan, R. Quinlan, and A. N. Yaroslavsky, "Polarization-sensitive multimodal imaging for detecting breast cancer," Cancer Res. **74**, 4685–4693 (2014).
13. Z. Li, M. Rupinski, J. Zetterberg, Z. Alwahabi, and M. Aldén, "Detection of methane with mid-infrared polarization spectroscopy," Appl. Phys. B **79**, 135–138 (2004).
14. G. Yang and Y. Xu, "Vibrational circular dichroism spectroscopy of chiral molecules," in *Electronic and Magnetic Properties of Chiral Molecules and Supramolecular Architectures* (Springer, 2010), pp. 189–236.
15. B. Guo, Y. Wang, C. Peng, H. Zhang, G. Luo, H. Le, C. Gmachl, D. L. Sivco, M. L. Peabody, and A. Y. Cho, "Laser-based mid-infrared reflectance imaging of biological tissues," Opt. Express **12**, 208–219 (2004).
16. P. Bassan, M. J. Weida, J. Rowlette, and P. Gardner, "Large scale infrared imaging of tissue micro arrays (TMAs) using a tunable quantum cascade laser (QCL) based microscope," Analyst **139**, 3856–3859 (2014).
17. F. A. Sadjadi and C. S. Chun, "Passive polarimetric IR target classification," IEEE Trans. Aerosp. Electron. Syst. **37**, 740–751 (2001).
18. N. Short, S. Hu, P. Gurram, K. Gurton, and A. Chan, "Improving cross-modal face recognition using polarimetric imaging," Opt. Lett. **40**, 882–885 (2015).
19. K. P. Gurton, A. J. Yuffa, and G. W. Videen, "Enhanced facial recognition for thermal imagery using polarimetric imaging," Opt. Lett. **39**, 3857–3859 (2014).
20. B. Schaefer, E. Collett, R. Smyth, D. Barrett, and B. Fraher, "Measuring the Stokes polarization parameters," Am. J. Phys. **75**, 163–168 (2007).
21. Z. Wu, P. E. Powers, A. M. Sarangan, and Q. Zhan, "Optical characterization of wiregrid micropolarizers designed for infrared imaging polarimetry," Opt. Lett. **33**, 1653–1655 (2008).
22. A. G. Andreou and Z. K. Kalayjian, "Polarization imaging: principles and integrated polarimeters," IEEE Sens. J. **2**, 566–576 (2002).
23. T. Tokuda, S. Sato, H. Yamada, K. Sasagawa, and J. Ohta, "Polarisation-analysing CMOS photosensor with monolithically embedded wire grid polariser," Electron. Lett. **45**, 228–230 (2009).

24. X. Zhao, F. Boussaid, A. Bermak, and V. G. Chigrinov, "Thin photo-patterned micropolarizer array for CMOS image sensors," IEEE Photon. Technol. Lett. **21**, 805–807 (2009).
25. V. Gruev, A. Ortu, N. Lazarus, J. Van der Spiegel, and N. Engheta, "Fabrication of a dual-tier thin film micropolarization array," Opt. Express **15**, 4994–5007 (2007).
26. K. E. Shopsowitz, H. Qi, W. Y. Hamad, and M. J. MacLachlan, "Free-standing mesoporous silica films with tunable chiral nematic structures," Nature **468**, 422–425 (2010).
27. V. Gruev, R. Perkins, and T. York, "CCD polarization imaging sensor with aluminum nanowire optical filters," Opt. Express **18**, 19087–19094 (2010).
28. J. J. Wang, L. Chen, X. Liu, P. Sciortino, F. Liu, F. Walters, and X. Deng, "30-nm-wide aluminum nanowire grid for ultrahigh contrast and transmittance polarizers made by UV-nanoimprint lithography," Appl. Phys. Lett. **89**, 141105 (2006).
29. J. J. Wang, F. Walters, X. Liu, P. Sciortino, and X. Deng, "High-performance, large area, deep ultraviolet to infrared polarizers based on 40 nm line/78 nm space nanowire grids," Appl. Phys. Lett. **90**, 061104 (2007).
30. N. Lefaudeux, N. Lechocinski, S. Breugnot, and P. Clemenceau, "Compact and robust linear Stokes polarization camera," Proc. SPIE **6972**, 69720B (2008).
31. D. A. Coleman, J. Fernsler, N. Chattham, M. Nakata, Y. Takanishi, E. Korblova, D. R. Link, R. F. Shao, W. G. Jang, J. E. Maclennan, O. Mondainn-Monval, C. Boyer, W. Weissflog, G. Pelzl, L. C. Chien, J. Zasadzinski, J. Watanabe, D. M. Walba, H. Takezoe, and N. A. Clark, "Polarization-modulated smectic liquid crystal phases," Science **301**, 1204–1211 (2003).
32. E. M. Sánchez-Carnerero, F. Moreno, B. L. Maroto, A. R. Agarrabeitia, M. J. Ortiz, B. G. Vo, G. Muller, and S. de la Moya, "Circularly polarized luminescence by visible-light absorption in a chiral O-BODIPY dye: unprecedented design of CPL organic molecules from achiral chromophores," J. Am. Chem. Soc. **136**, 3346–3349 (2014).
33. J. K. Gansel, M. Thiel, M. S. Rill, M. Decker, K. Bade, V. Saile, G. von Freymann, S. Linden, and M. Wegener, "Gold helix photonic metamaterial as broadband circular polarizer," Science **325**, 1513–1515 (2009).
34. B. Frank, X. Yin, M. Schäferling, J. Zhao, S. M. Hein, P. V. Braun, and H. Giessen, "Large-area 3D chiral plasmonic structures," ACS Nano **7**, 6321–6329 (2013).
35. M. Decker, M. Klein, M. Wegener, and S. Linden, "Circular dichroism of planar chiral magnetic metamaterials," Opt. Lett. **32**, 856–858 (2007).
36. W. Li, Z. J. Coppens, L. V. Besteiro, W. Wang, A. O. Govorov, and J. Valentine, "Circularly polarized light detection with hot electrons in chiral plasmonic metamaterials," Nat. Commun. **6**, 8379 (2015).
37. J. Hu, X. Zhao, Y. Lin, A. Zhu, X. Zhu, P. Guo, B. Cao, and C. Wang, "All-dielectric metasurface circular dichroism waveplate," Sci. Rep. **7**, 41893 (2017).
38. J. Dong, J. Zhou, T. Koschny, and C. Soukoulis, "Bi-layer cross chiral structure with strong optical activity and negative refractive index," Opt. Express **17**, 14172–14179 (2009).
39. F. Afshinmanesh, J. S. White, W. Cai, and M. L. Brongersma, "Measurement of the polarization state of light using an integrated plasmonic polarimeter," Nanophotonics **1**, 125–129 (2012).
40. Y. Zhao, M. Belkin, and A. Alù, "Twisted optical metamaterials for planarized ultrathin broadband circular polarizers," Nat. Commun. **3**, 870 (2012).
41. Y. Zhao, A. N. Askarpour, L. Sun, J. Shi, X. Li, and A. Alù, "Chirality detection of enantiomers using twisted optical metamaterials," Nat. Commun. **8**, 14180 (2017).
42. A. Pors, M. G. Nielsen, and S. I. Bozhevolnyi, "Plasmonic metagratings for simultaneous determination of Stokes parameters," Optica **2**, 716–723 (2015).
43. W. T. Chen, P. Torok, M. R. Foreman, C. Y. Liao, W. Y. Tsai, P. R. Wu, and D. P. Tsai, "Integrated plasmonic metasurfaces for spectropolarimetry," Nanotechnology **27**, 224002 (2016).
44. E. Arbabi, S. M. Kamali, A. Arbabi, and A. Faraon, "Full-Stokes imaging polarimetry using dielectric metasurfaces," ACS Photon. **5**, 3132–3140 (2018).
45. Z. Y. Yang, Z. K. Wang, Y. X. Wang, X. Feng, M. Zhao, Z. J. Wan, L. Q. Zhu, J. Liu, Y. Huang, J. S. Xia, and M. Wegener, "Generalized Hartmann-Shack array of dielectric metalens sub-arrays for polarimetric beam profiling," Nat. Commun. **9**, 4607 (2018).
46. H. Yang, G. H. Li, G. T. Cao, Z. Y. Zhao, J. Chen, K. Ou, X. S. Chen, and W. Lu, "N broadband polarization resolving based on dielectric metalenses in the near-infrared," Opt. Express **26**, 5632–5643 (2018).
47. M. Jung, S. Dutta-Gupta, N. Dabidian, I. Brener, M. Shcherbakov, and G. Shvets, "Polarimetry using graphene-integrated anisotropic metasurfaces," ACS Photon. **5**, 4283–4288 (2018).
48. H. G. Berry, G. Gabrielse, and A. E. Livingston, "Measurement of the Stokes parameters of light," Appl. Opt. **16**, 3200–3205 (1977).
49. T.-H. Chiou, S. Kleinlogel, T. Cronin, R. Caldwell, B. Loeffler, A. Siddiqi, A. Goldizen, and J. Marshall, "Circular polarization vision in a stomatopod crustacean," Curr. Biol. **18**, 429–434 (2008).
50. I. M. Daly, M. J. How, J. C. Partridge, S. E. Temple, N. J. Marshall, T. W. Cronin, and N. W. Roberts, "Dynamic polarization vision in mantis shrimps," Nat. Commun. **7**, 12140 (2016).
51. M. F. Land and D. Osorio, "Extraordinary color vision," Science **343**, 381–382 (2014).
52. N. F. Yu, P. Genevet, M. A. Kats, F. Aieta, J. P. Tetienne, F. Capasso, and Z. Gaburro, "Light propagation with phase discontinuities: generalized laws of reflection and refraction," Science **334**, 333–337 (2011).